Multiphase coherent nanointerface network enhances thermoelectric performance for efficient energy conversion and contactless thermosensation applications in GeTe

Jianglong Zhu, Xiaobo Tan, Min Hong, Yanxing Wei, Huangshui Ma, Fan Feng, Yuange Luo, Hao Wu, Qiang Sun*, Ran Ang*

J. L. Zhu, X.B Tan, F. Feng, Y.G. Luo, R. Ang
Key Laboratory of Radiation Physics and Technology, Ministry of Education, Institute of Nuclear Science and Technology, Sichuan University, Chengdu 610064, China
Y.X. Wei, H.S. Ma, Q. Sun
State Key Laboratory of Oral Diseases, National Clinical Research Center for Oral Diseases, West China Hospital of Stomatology, Sichuan University, Chengdu, Sichuan 610041, China
M. Hong
Centre for Future Materials, University of Southern Queensland, Springfield Campus, QLD, 4300, Australia
Y.X. Wei, H.S. Ma, Q. Sun
Sichuan Provincial Engineering Research Center of Oral Biomaterials, Chengdu, Sichuan 610041, China
H. Wu
Department of Stomatology, the First Medical Centre, Chinese PLA General Hospital, Beijing 100853, China
R. Ang
Institute of New Energy and Low-Carbon Technology, Sichuan University, Chengdu 610065, China
*Correspondence and requests for materials should be addressed to R.A. (email: rang@scu.edu.cn) or Q.S. (email: qiangsun@scu.edu.cn)

Keywords: thermoelectrics, GeTe, coherent interfaces, energy conversion, photo-thermoelectric effect

ABSTRACT

Counter doping is a prevalent strategy to optimize the excessively high carrier concentration in GeTe, while it may impair carrier transport and reduce mobility, thereby limiting the potential to improve *ZT*. Herein, we propose a novel approach to overcome this challenge. A multiphase coherent nanointerface network, formed between pseudo-cubic GeTe, Cu_2Te, and PbTe phases, with effective Cu ions delocalization, has been realized in Cu_2Te alloyed $Ge_{0.84}Cd_{0.06}Pb_{0.10}Te$. This design selectively modulates both charge carrier and phonon transport, resulting in increased mobility and optimized carrier concentration that contribute to enhanced power factor, with an ultra-low lattice thermal conductivity of ~0.33 W m^{-1} K^{-1} at 653 K. Consequently, the peak *ZT* of ~2.22 at 803 K and average *ZT* of ~1.40 from 303 to 803 K is achieved in $(Ge_{0.84}Cd_{0.06}Pb_{0.10}Te)_{0.99}(Cu_2Te)_{0.01}$. Furthermore, the novel structural modulation results in robust mechanical properties. Utilizing these optimized materials, achieving a high power density of ~1.47 W cm^{-2} at a temperature difference of 400 K in the fabricated 7-pair thermoelectric module. Moreover, a thermoelectric energy harvesting array device is assembled, exhibiting potential for applications in non-radiative energy harvesting from lasers and touchless thermosensation, further advancing the applications of thermoelectric materials and devices.

Keywords: thermoelectrics, GeTe, coherent interfaces, energy conversion, photo-thermoelectric effect

1. Introduction

Thermoelectric (TE) technology, capable of directly converting thermal and electrical energy, provides a means to harness a significant portion of waste heat generated during energy consumption, transforming it into electrical energy to realize carbon neutrality.[1] The performance of TE materials limits the maximum conversion efficiency η_{max} of TE technology, which is determined by the dimensionless figure of merit ZT, defined as $ZT = S^2\sigma T/\kappa$, where S, σ, T, and κ refer to the Seebeck coefficient, the electrical conductivity, the absolute temperature, and the total thermal conductivity (comprising both electronic thermal conductivity κ_{ele} and lattice thermal conductivity κ_{lat}),[2,3] respectively. Therefore, striking a balance between the carrier (power factor, $PF=S^2\sigma$) and phonon (κ_{lat}) transport properties, which are strongly coupled, presents an ideal strategy for attaining higher ZT values.[4–7]

Among the numerous TE materials, the eco-friendly GeTe stands out due to its exceptional performance, making it a viable candidate for medium-temperature power generation.[8,9] Some effective strategies have been proven to improve the performance of GeTe-based TE materials. Trivalent elements such as Sb[10] and Bi[11] are commonly doped to provide additional electrons, optimizing the excessively high carrier concentration n_H caused by the Ge vacancies in GeTe. Conversely, alloying with PbSe,[12] Cu_2Te,[13] and $NaSbTe_2$[14] can inhibit the formation of Ge vacancies, thereby reducing n_H. To enhance the electronic band structure by increasing effective mass m^*, elements such as Cd,[15] Mn,[16] and Sn[17] are doped to achieve band convergence by reducing the energy offset (ΔE) between light band (L band) and heavy band (Σ band) of GeTe. Meanwhile, the resonant level induced by In[18,19] doping can potentially distort the electronic density of states near the Fermi level. However, the process of doping inevitably introduces defects of various dimensions, the most common being point defects and nanoprecipitates. These defects, with phonon-free paths smaller than the phonon, can enhance phonon scattering and reduce κ_{lat}.[20,21] Nevertheless, the increase in effective mass or the introduction of

nanostructures such as nanoprecipitates and defects could easily impair carrier transport, leading to a decrease in mobility μ, thereby limiting the enhancement of ZT.[22,23]

Here, we introduce a novel multiphase coherent nanointerface network constructed in Cu_2Te alloyed $Ge_{0.84}Cd_{0.06}Pb_{0.10}Te$. This network allows for flawless passage of charge carriers, thereby significantly enhancing the TE performance for energy conversion and touchless thermosensation applications. Specifically, Cu_2Te alloying further optimizes the n_H without altering the band structure. This is facilitated by a coherent interface network formed through the mutual interaction of Cu_2Te, PbTe, and GeTe, and the delocalization of Cu ions, resulting in an improvement in μ and PF. Moreover, the established multiphase nanostructures and the softening of chemical bonds due to Cu_2Te-alloyed lead to an ultra-low κ_{lat} of ~0.33 W m^{-1} K^{-1} at 653 K in $(Ge_{0.84}Cd_{0.06}Pb_{0.10}Te)_{0.99}(Cu_2Te)_{0.01}$. As a result, a high ZT of ~2.22 at 803 K and an average ZT_{ave} of ~1.40 (303–803 K) are achieved in $(Ge_{0.84}Cd_{0.06}Pb_{0.10}Te)_{0.99}(Cu_2Te)_{0.01}$. With enhanced hardness and compressive properties, the corresponding 7-pair TE module displays a power density P_d of ~1.47 W cm^{-2} and a maximum conversion efficiency η_{max} of ~ 7.0% at a temperature difference ΔT of 400 K. Furthermore, we have developed a unique TE energy harvesting device that exhibits superior performance in nonradiative harvesting of laser energy and contactless thermosensation, providing a potential application in GeTe-based TE materials.

2. Results and Discussion

2.1. Phase Identification and Microstructure Characterizations

The X-ray diffraction (XRD) of the as-prepared $(Ge_{0.84}Cd_{0.06}Pb_{0.10}Te)_{1-x}(Cu_2Te)_x$ (x=0–0.02) was conducted to identify the phase composition and displayed in Figure S1a. All characteristic diffraction peaks align well with the rhombohedral GeTe phase (*r*-GeTe, PDF #00–47-1079), indicating a tendency to transition from *r*-GeTe to cubic GeTe phase (*c*-GeTe). This observation is confirmed by the slight shift of the diffraction peak towards a lower 2θ as the content of Cu_2Te increases (Figure S1b), and the lattice parameters α increase, which is

caused by the larger ionic radii of Cu^{+1} (~0.77 Å) compared to Ge^{2+} (~0.73 Å). Concurrently, the gradual convergence of the diffraction peak at 2θ=41°-43° and the increase in interaxial angles α in r-GeTe are noted (Figure S1c,d). Differential scanning calorimetry (DSC) measurements reveal that the phase transition temperature (T_c) of $(Ge_{0.84}Cd_{0.06}Pb_{0.10}Te)_{0.99}(Cu_2Te)_{0.01}$ is 673 K (Figure S2), and an additional T_c from δ (hexagonal) to ε (cubic) of Cu_2Te appears at 752 K,[24] indicating the potential presence of cubic Cu_2Te phases in the matrix. To further determine the valence state of Cu in $(Ge_{0.84}Cd_{0.06}Pb_{0.10}Te)_{0.99}(Cu_2Te)_{0.01}$, X-ray photoelectron spectroscopy (XPS) was performed. The full scan XPS results for the elements Cd, Pb, and Cu are presented in Figure S3a. The detailed XPS scan of Cu confirms that the valence state of Cu is +1 (Figure S3b)[25,26], in agreement with the XRD analysis.

To gain a comprehensive understanding of how Cu_2Te alloying impacts the microstructure and crystallography of the matrix, as well as its modulating effect on phonon and carrier transport, the scanning transmission electron microscopy (STEM) characterization was carried out on $(Ge_{0.84}Cd_{0.06}Pb_{0.10}Te)_{0.99}(Cu_2Te)_{0.01}$ sample. As shown in **Figure 1**a, various nanoscale precipitates with different contrasts are randomly dispersed in the matrix. The corresponding EDS reveals that there are primarily three different types of nanoprecipitates, namely Cu_2Te, PbTe, and Ge. Among these foreign phases, the Pb-enriched phase, identified as PbTe based on the chemical composition, exhibits an elongated morphology resulting from phase separation.[27] Given the valence state of Cu^{+1} and the low solid solution limit of Cu in GeTe, the Cu-enriched phase can be identified as Cu_2Te.[26] The bright-filed TEM image (**Figure 1**b) illustrates a region of the Cu_2Te nanoprecipitate and matrix with planar defects. **Figure 1**c presents the selected area electron diffraction (SAED) pattern obtained from the area circled in yellow in **Figure 1**b, which clarifies the orientation relationship at the phase boundary. The orientation relationship of $Cu_2Te(112)//GeTe(111)$ is confirmed by indexing the overlapping diffraction

patterns. **Figure 1**d,e displays magnified images of the GeTe matrix and Cu_2Te phase regions in Figure 1b, as well as the corresponding fast Fourier transform (FFT) pattern. Notably, the measured interplanar spacings of ~3.5 Å and ~2.1 Å align well with the $(\bar{1}\bar{1}0)$ and $(2\bar{2}0)$ planes of Cu_2Te phase, respectively. In **Figure 1**e, the {220} plane of *r*-GeTe with a spacing of ~2.1 Å can be observed. Therefore, a highly coherent interface can be formed between Cu_2Te and GeTe, given the small lattice mismatch. Interestingly, coherent interfaces of *r*-GeTe and *ε*-Cu_2Te are also observed in different regions of this sample (Figure S4-5). **Figure 1**f illustrates the schematic atomic model and explains the formation of a coherent interface between the doped GeTe matrix and the Cu_2Te phase along the zone axis indicated by Figure 1c.

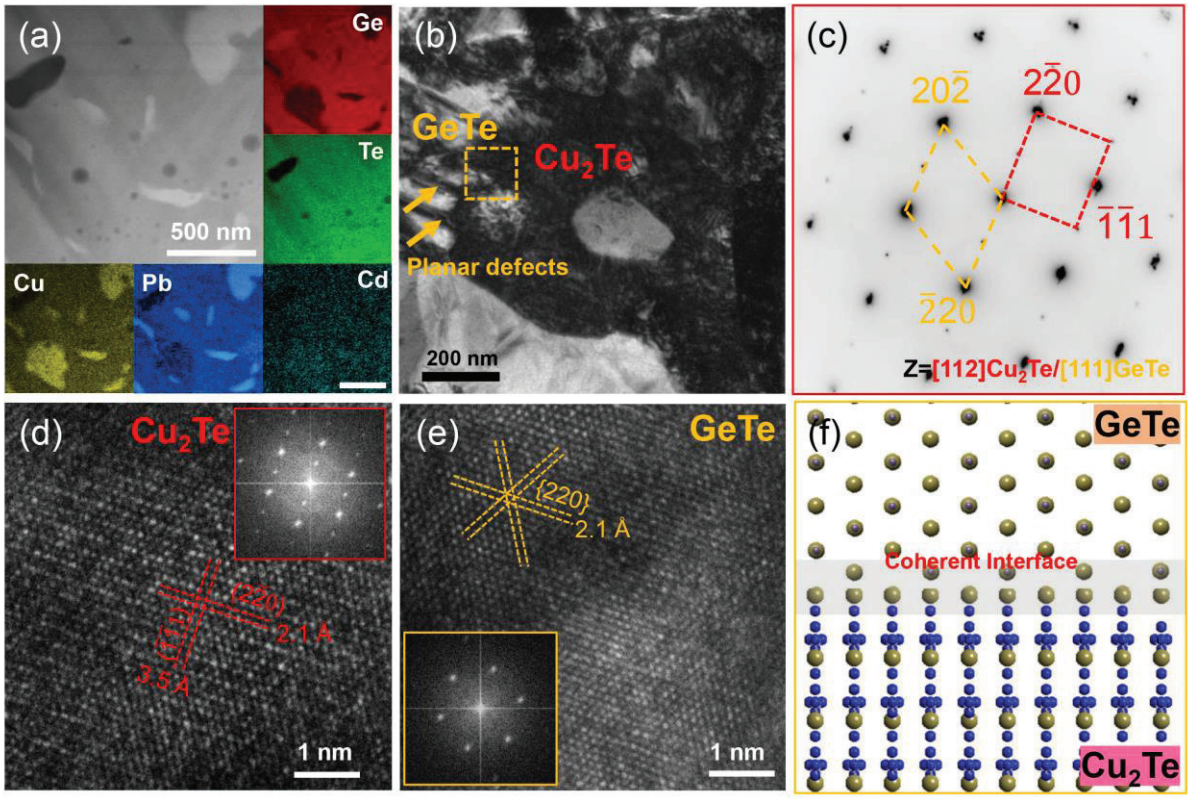

Figure 1 Coherent nanointerface between Cu_2Te and GeTe nanoprecipitates for the $(Ge_{0.84}Cd_{0.06}Pb_{0.10}Te)_{0.99}(Cu_2Te)_{0.01}$ sample. a) Low-magnification STEM image and corresponding EDS elemental maps. b) A low-magnification bright-field TEM image of the corresponding area of (a), showing the planar defects of the GeTe matrix. c) The diffraction spots of the Cu_2Te phase along the [112] direction and the overlapped diffraction pattern of the GeTe phase along the [111] direction, marked in yellow. d, e)

HRTEM image of Cu_2Te and GeTe, magnified by the marked region in (b), respectively. f) The schematic of the coherent phase interface between Cu_2Te and GeTe.

Further characterization indicates that a relatively high proportion of the Cu_2Te nanoprecipitates observed in the GeTe matrix may preferentially co-precipitate within the PbTe nanoprecipitates. As revealed by the dark-field STEM imaging, **Figure 2**a,b depicts a substantial quantity of banded PbTe precipitates distributed in the matrix, with smaller nanoscale strip/layered structures appearing nearby, suggesting that the interfaces can serve as the origin of defects. Moreover, Cu_2Te nanoparticles distributed near the PbTe phase are observed. A small number of Cu atoms have entered the PbTe lattice to form a Cu-doped PbTe phase, because the Cu atoms are small enough to form point defects in PbTe.[28,29] Careful indexing of the overlapping diffraction patterns at the interface between the PbTe and Cu_2Te phases demonstrates that the *d*-spacing between them is very similar, leading to the formation of a coherent interface (**Figure 2**c). **Figure 2**d enlarges a selected area with a herringbone domain structure. A layered sandwich structure is formed in this region, with the matrix containing planar defects/interfaces, closely connected defects (areas of lattice distortion), and PbTe phases, reflecting the evolution process of defects. Further magnification of the interface region and the ~3% lattice mismatch between the parallel planes of PbTe and GeTe phases prove the formation of a coherent interface (**Figure 2**e-g). The doped GeTe adopts a pseudo-cubic structure, as revealed by the previous XRD analysis. Additionally, a high-quality coherent interface has also been established between the ε-Cu_2Te and PbTe phases (**Figure 2**h,i). Therefore, Cu_2Te alloying has modulated the evolution of defect formation in the $Ge_{0.84}Cd_{0.06}Pb_{0.10}Te$ matrix by: 1) introducing various nanophase heterojunctions, 2) forming a sandwich-like layered defect structure, and 3) constructing a novel multiphase coherent nanointerface network. The corresponding schematic atomic model is displayed in **Figure 2**j.

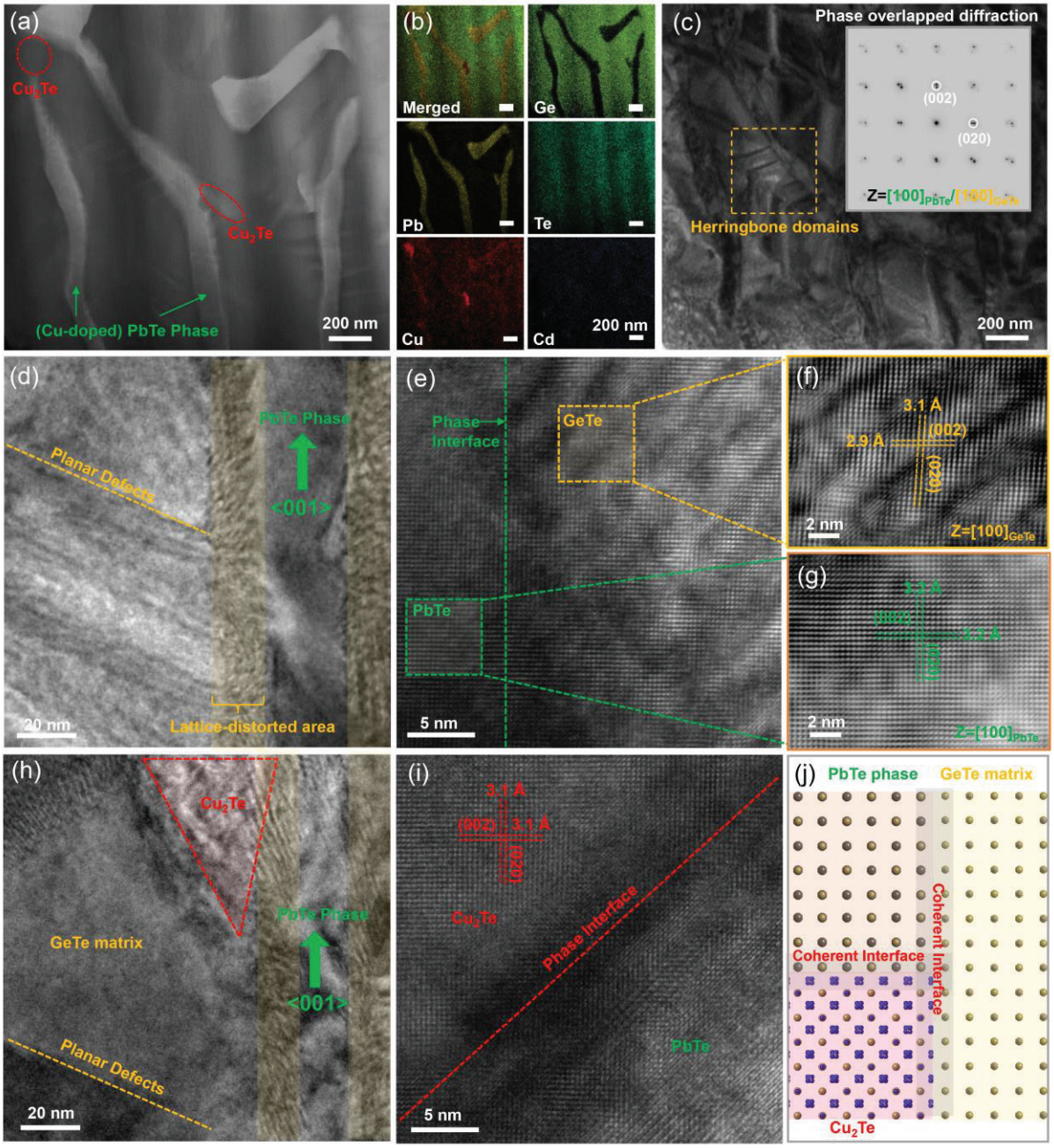

Figure 2 Structural characteristics of multiphase coherent nanointerface network for the $(Ge_{0.84}Cd_{0.06}Pb_{0.10}Te)_{0.99}(Cu_2Te)_{0.01}$ sample. a) Low-magnification STEM image and b) corresponding EDS elemental maps. c) A low-magnification TEM image of the herringbone domain and SAED image obtained from the PbTe and GeTe phases, indicating the highly coherent interfaces. d) HRTEM image magnified by the marked region in (c), showing the distribution of PbTe and Cu_2Te in GeTe. (e) HRTEM image of an interface between PbTe and GeTe obtained from (d). f, g) HRTEM image of PbTe and GeTe, magnified by the marked region in (e), respectively. h) HRTEM image of multiphase and defect evolution area. i) HRTEM

image of an interface between ε-Cu_2Te and PbTe. j) The schematic of the multiphase coherent nanointerface network between ε-Cu_2Te, PbTe, and pseudo-cubic GeTe.

In fact, incorporating nanostructures into TE materials commonly results in incoherent interfaces, which enhance carrier scattering and reduce carrier mobility due to substantial lattice mismatch and high interface energy at the phase boundary. Thus, it is desirable to construct semi-coherent and/or coherent nanointerface structures with smaller lattice mismatches. This can effectively decrease the interfacial energy in TE materials, ensuring optimal transmission of carriers and strong phonon scattering.[30] Excitingly, the multiphase coherent nanointerface network in $(Ge_{0.84}Cd_{0.06}Pb_{0.10}Te)_{1-x}(Cu_2Te)$ provides an unparalleled conductive network medium for the transport of charge carriers.

The carrier transport properties of $(Ge_{0.84}Cd_{0.06}Pb_{0.10}Te)_{1-x}(Cu_2Te)_x$ at room temperature are summarized in Figure S6. With increasing the Cu_2Te fraction, the carrier concentration n_H decreases, which is attributed to the increase in Ge vacancy formation energy induced by Cu_2Te alloying.[13] As the temperature rises to 503 K (Figure 3a), the rapidly increasing n_H is due to a reduction in phase transition temperature (Figure S3). It should be noted that when $x \geq 0.01$, the n_H remains almost constant, while carrier mobility μ shows an unexpected linear increase. The temperature-dependent μ of all samples adheres to the $T^{-3/2}$ trend, confirming that acoustic phonon scattering is the primary carrier scattering mechanism (Figure 3b), the increase of μ is independent of the scattering mechanism.

For a deeper understanding of the impact of Cu_2Te-alloying on charge transport characteristics, we theoretically calculated μ as a function of n_H for experimental values and representative GeTe systems [31,32,15,33,34] at 303 K, using the single parabolic band (SPB) model (Figure 3c). Due to the large effective mass m^* of $Ge_{0.84}Cd_{0.06}Pb_{0.10}Te$ in the valence band, its theoretical μ (red curve) is lower than the theoretical value of the pristine GeTe (black curve). The experimental μ of $Ge_{0.84}Cd_{0.06}Pb_{0.10}Te$ fell below the theoretical curve owing to the

introduction of additional point defects. However, the experimental μ of $(Ge_{0.84}Cd_{0.06}Pb_{0.10}Te)_{1-x}(Cu_2Te)_x$ exceeds theoretical predictions as the Cu_2Te content increases. It is higher than $Ge_{0.84-x}Cd_{0.06}Pb_{0.10}Sb_xTe$[15] with similar n_H, and even closer to $Ge_{1-x}Cd_xTe$[32] and $Ge_{1-x}Pb_xTe$[31]. This contradicts the general semiconductor physics principle that a larger effective mass corresponds to heavier charge carriers and lower drift mobility.[35] Therefore, the multiphase coherent nanointerface network in $(Ge_{0.84}Cd_{0.06}Pb_{0.10}Te)_{1-x}(Cu_2Te)_x$ plays a crucial role in charge carrier effective transport, acting as a conductive network medium to promote perfect carrier transport and ultimately improve μ.

Two-dimensional mapping of the calculated electron localization function (ELF) for the rhombic and cubic phases of $Ge_{0.84}Cd_{0.06}Pb_{0.10}Te$ and $(Ge_{0.84}Cd_{0.06}Pb_{0.10}Te)_{0.99}(Cu_2Te)_{0.01}$ are plotted (Figure 3d and Figure S7) to further comprehend the regulatory effect of introducing Cu_2Te on chemical bonding. The corresponding crystal structure is shown in Figure S8. The ELF of 1 corresponds to strong electron localization, while a decrease to 0 indicates electron delocalization, as depicted by a color bar from red to blue. In both rhombic and cubic phases, electron delocalization zones with an ELF close to 0 were formed by Cu_2Te alloying. Dispersed circular domains with a blue color were observed around the Cu atom, indicating an obvious degree of electron delocalization near the Cu atom,[36] which could be an additional critical factor contributing to the increase of μ in $(Ge_{0.84}Cd_{0.06}Pb_{0.10}Te)_{1-x}(Cu_2Te)_x$.

The temperature-dependent σ of $(Ge_{0.84}Cd_{0.06}Pb_{0.10}Te)_{1-x}(Cu_2Te)_x$ is depicted in Figure 3e. The addition of Cu_2Te suppresses the formation of Ge vacancies, thereby reducing n_H and σ. However, as the Cu_2Te content increases, the synergy of the established multiphase coherent nanointerface network and the effect of delocalization increases μ, leading to a slight enhancement of σ. All S of the Cu_2Te-alloying samples exhibit enhancement in the entire temperature range (Figure 3f). The peak S of $(Ge_{0.84}Cd_{0.06}Pb_{0.10}Te)_{0.99}(Cu_2Te)_{0.01}$ is ~ 265 μV K^{-1} at 503 K. Despite a decrease, S can be maintained over ~200 μV K^{-1} up to 803 K due to the

phase transition. The theoretical calculation of n_H-dependent S at room temperature, based on the SPB mode is illustrated in Figure 3g. Effective band convergence pushes the m^* over 2.0 m_e in the $Ge_{0.84}Cd_{0.06}Pb_{0.10}Te$ matrix,[15,32,37] and with the introduction of Cu_2Te, there is no change in m^*, as reported in GeTe-$x$$Cu_2Te$[13] and $Ge_{1-2x}Cu_{2x}Te$[33], indicating that Cu_2Te cannot modulate the band structure of GeTe. The density functional theory (DFT) calculations for the rhombic and cubic phases of $Ge_{0.84}Cd_{0.06}Pb_{0.10}Te$ and $(Ge_{0.84}Cd_{0.06}Pb_{0.10}Te)_{0.99}(Cu_2Te)_{0.01}$ further theoretically confirm that the influence of Cu_2Te on the electronic band structure of GeTe is negligible (Figure 3h,i and Figure S9). Therefore, the optimized n_H by Cu_2Te alloying enhances the S of $(Ge_{0.84}Cd_{0.06}Pb_{0.10}Te)_{1-x}(Cu_2Te)_x$. The multiphase coherent nanointerface network and effective delocalization, both induced by Cu_2Te alloying, lead to optimized n_H and enhanced μ. This collaboration ensures that the PF remains at a high value (Figure S10).

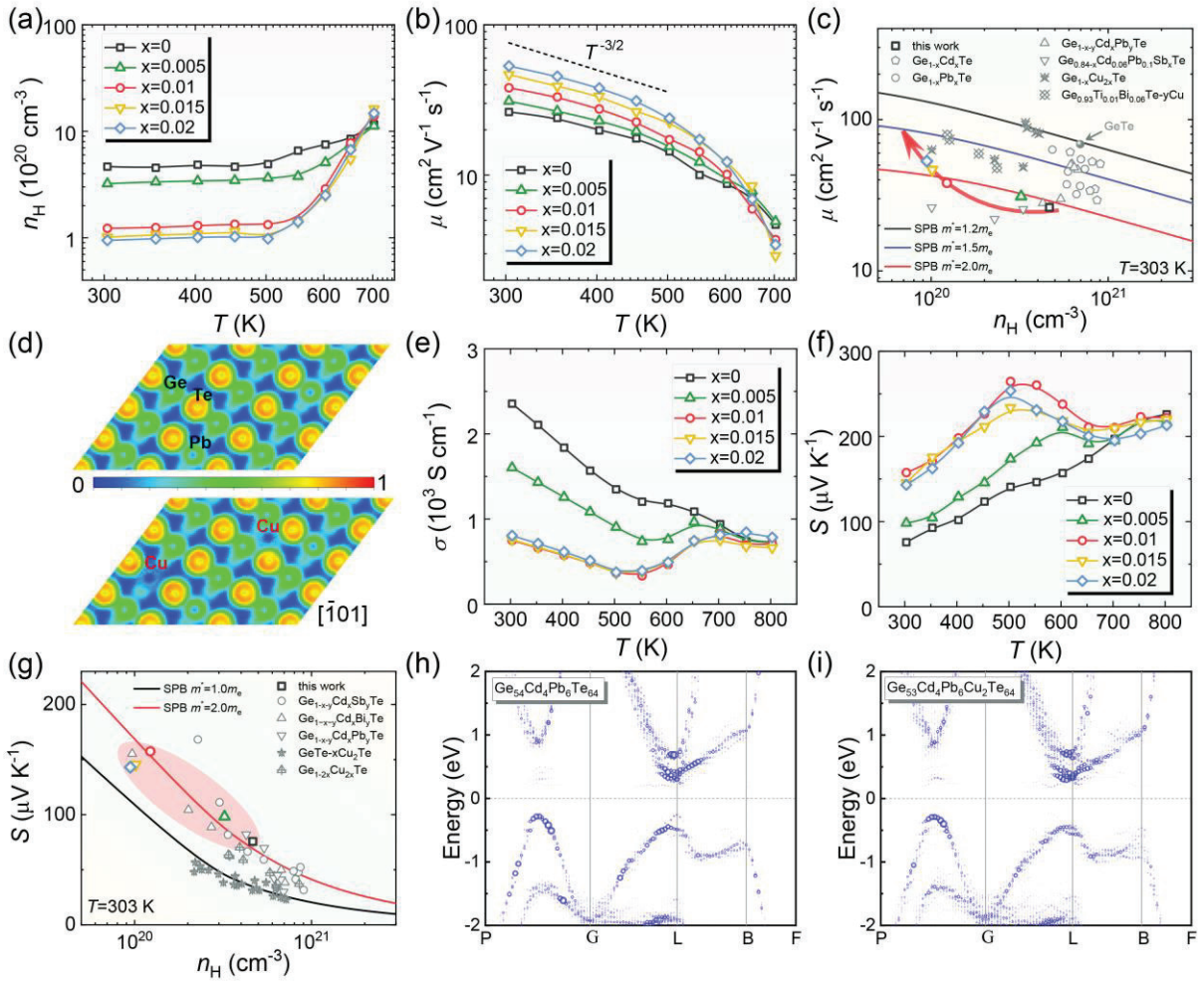

Figure 3 The electrical transport properties for $(Ge_{0.84}Cd_{0.06}Pb_{0.10}Te)_{1-x}(Cu_2Te)_x$. Temperature-dependent a) n_H and b) μ, c) n_H-dependent μ at 303 K, with a comparison to some typical GeTe-based TE materials.[31,32,15,33,34] d) 2D mappings of the calculated ELF for *r*-$Ge_{0.84}Cd_{0.06}Pb_{0.10}Te$ and *r*-$(Ge_{0.84}Cd_{0.06}Pb_{0.10}Te)_{0.99}(Cu_2Te)_{0.01}$. Temperature-dependent e) σ and f) S of $(Ge_{0.84}Cd_{0.06}Pb_{0.10}Te)_{1-x}(Cu_2Te)_x$. g) n_H-dependent S in comparison with literature results.[13,15,32,33,37] Band structure calculated for h) *r*-$Ge_{0.84}Cd_{0.06}Pb_{0.10}Te$ and i) *r*-$(Ge_{0.84}Cd_{0.06}Pb_{0.10}Te)_{0.99}(Cu_2Te)_{0.01}$.

Figure S11a presents the temperature-dependent κ of $(Ge_{0.84}Cd_{0.06}Pb_{0.10}Te)_{1-x}(Cu_2Te)_x$. The total κ sharply decreases to ~ 1.24 W m^{-1} K^{-1} for $(Ge_{0.84}Cd_{0.06}Pb_{0.10}Te)_{0.99}(Cu_2Te)_{0.01}$ at 303 K, with an average κ of ~ 1.12 W m^{-1} K^{-1} in 303–803 K. The decrease in σ leads to a decrease in κ_{ele} (Figure S11b,c), contributing to a partial reduction in total κ. Moreover, the reduced κ_{lat} is shown in Figure 4a. Interestingly, the reduction in κ_{lat} due to Cu_2Te alloying is not evident in the low-temperature range, but as the temperature increases, the κ_{lat} of $(Ge_{0.84}Cd_{0.06}Pb_{0.10}Te)_{1-x}(Cu_2Te)_x$ decreases, possibly due to the enhanced phonon scattering by delocalized Cu atoms with increasing temperature.[29,38] The ultra-low κ_{lat} is ~0.33 W m^{-1} K^{-1} at 653 K in $(Ge_{0.84}Cd_{0.06}Pb_{0.10}Te)_{0.99}(Cu_2Te)_{0.01}$, a 45% reduction compared to $Ge_{0.84}Cd_{0.06}Pb_{0.10}Te$, which is remarkably lower than most advanced GeTe systems (Figure 4b).[26,32–34,37,39]

The Debye Callaway model[40] is employed to further understand the role of phonon scattering sources (Figure 4c). Evidently, for the $(Ge_{0.84}Cd_{0.06}Pb_{0.10}Te)_{0.99}(Cu_2Te)_{0.01}$ sample, the influence of Umklapp and normal processes (UN), grain boundary (GB), and point defects (PD) as the primary scattering sources for κ_{lat} is relatively limited. The scattering sources due to stacking fault (SF), which affects mid-frequency phonons, drastically reduce the calculated κ_{lat} (green curve). Notably, with the additional phonon scattering source of nano precipitates ($NP_{(PbTe+Cu2Te)}$) introduced by Cu_2Te alloying, the calculated κ_{lat} (red curve) further decreases and aligns well with the experimental values. This highlights the important role of multiphase nanostructures in enhancing phonon scattering.

Fundamentally, due to the high sensitivity of Raman characteristics to the phase structure of GeTe, which can distinguish between *r*-GeTe and *c*-GeTe.[41,42] Raman measurements were carried out to further elucidate the "structure-property" relationship of the ultra-low κ_{lat} phenomenon. The Raman signal at random positions (Figure 4d) reveals that the $Ge_{0.84}Cd_{0.06}Pb_{0.10}Te$ sample exhibits representative peaks near 94 cm^{-1} (*E* mode) and 125 cm^{-1} (A_1 mode), indicative of typical *r*-GeTe.[43,44] As the introduction of Cu_2Te, $(Ge_{0.84}Cd_{0.06}Pb_{0.10}Te)_{0.99}(Cu_2Te)_{0.01}$ sample shows nearly no Raman peak, approaching the typical *c*-GeTe Raman mode, with enhanced cubic properties (Figure S1), leading to weakened chemical bonds and softened phonons. The decrease in sound speed with the increase of Cu_2Te content further confirms the weakening of chemical bonds (Figure S12) due to the delocalization of Cu. Hence, the evolution of defect structures driven by Cu_2Te intensely softens and scatters phonons, achieving an ultra-low κ_{lat}.

Owing to the weak electron-phonon coupling induced by multiphase coherent nanointerface network and effective delocalization, the *ZT* value of $(Ge_{0.84}Cd_{0.06}Pb_{0.10}Te)_{1-x}(Cu_2Te)_x$ remarkably raises in the entire temperature range (Figure 4e). The peak value of *ZT* and device *ZT* can reach ~2.22 and ~1.30 in $(Ge_{0.84}Cd_{0.06}Pb_{0.10}Te)_{0.99}(Cu_2Te)_{0.01}$ at 803 K, with an average ZT_{ave} of ~1.40 in the 303–803 K range. In addition, the repeatability test results demonstrate high repeatability in this work (Figure S13). Figure 4f plots the comparison of $(Ge_{0.84}Cd_{0.06}Pb_{0.10}Te)_{0.99}(Cu_2Te)_{0.01}$ in the 303-653 K range with other reported excellent GeTe materials,[26,32,33,37,45,46] surpassing most other Cu-alloyed GeTe.[26,33,45,46]

In addition to the high TE performance, the reliable mechanical properties are equally crucial for the fabrication and practical application of TE modules. We performed the room temperature Vickers microhardness and compressive tests to evaluate the mechanical properties of $(Ge_{0.84}Cd_{0.06}Pb_{0.10}Te)_{1-x}(Cu_2Te)_x$. With the introduction of Cu_2Te, the room-temperature Vickers microhardness H_v remarkably increases, improving from 175 H_v of $Ge_{0.84}Cd_{0.06}Pb_{0.10}Te$

to 227 H_v of $(Ge_{0.84}Cd_{0.06}Pb_{0.10}Te)_{0.99}(Cu_2Te)_{0.01}$, with a 30% increase. This is competitive with the reported GeTe materials (Figure 4g and Figure S14).[15,19,47–49] Moreover, the uniaxial compressive stress-strain curves are depicted in Figure 4h. Clearly, the compression strength increases from ~287 MPa for $Ge_{0.84}Cd_{0.06}Pb_{0.10}Te$ to ~350 MPa for $(Ge_{0.84}Cd_{0.06}Pb_{0.10}Te)_{0.99}(Cu_2Te)_{0.01}$, an enhancement of 22%, surpassing some typical brittle TE materials[50–55]. Similar to several metallic materials,[56,57] the compression strength exhibits an inverse relationship with strain. The high-strength GeTe obtained is attributed to the synergistic effect of the formation of a solid solution and multiphase precipitation by Cu_2Te alloying, which prevents crack propagation and improves mechanical strength,[58] with its strengthening mechanism shown in the inset in Figure 4h.

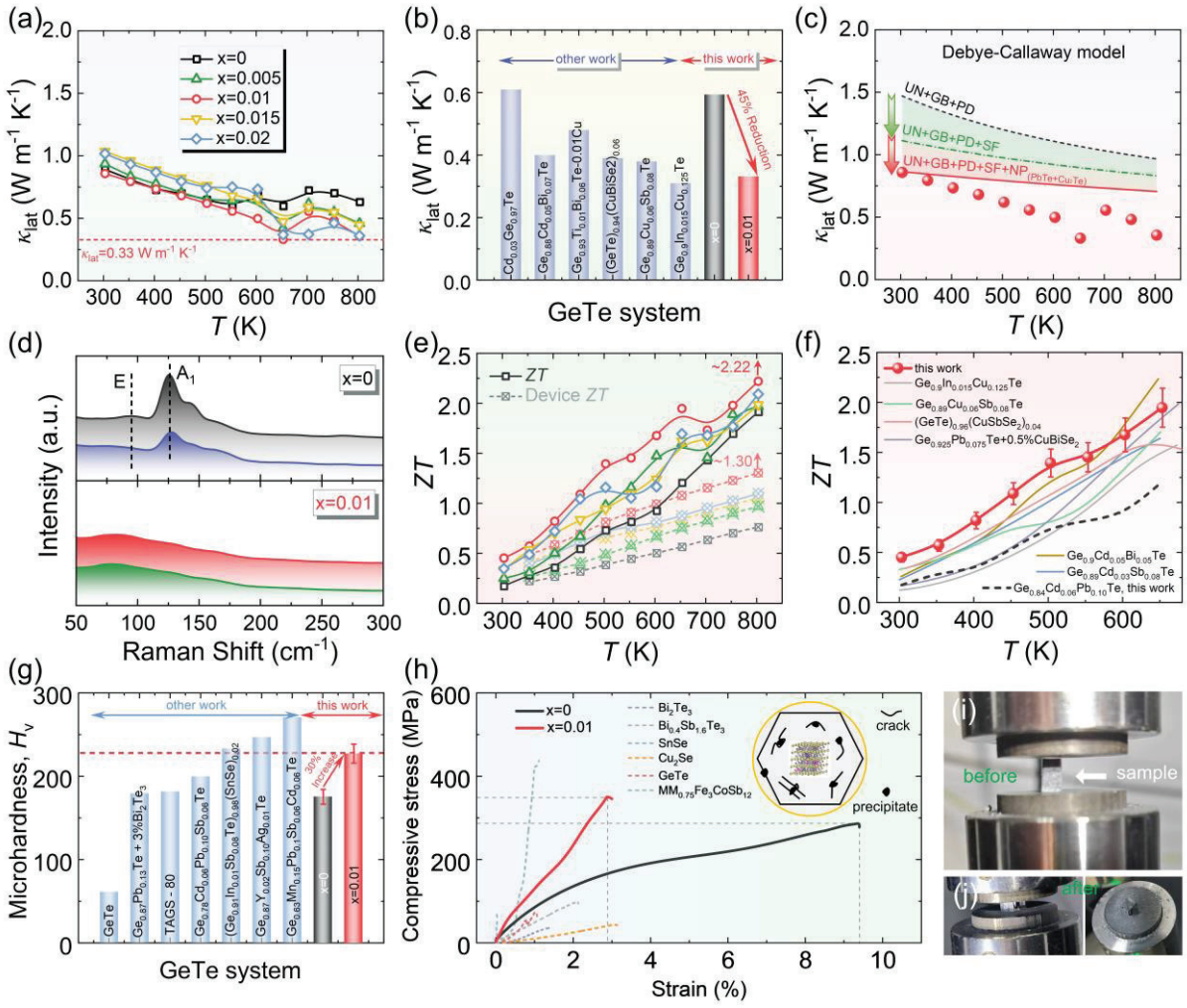

Figure 4 The thermal transport properties, TE performance, and mechanical properties for

$(Ge_{0.84}Cd_{0.06}Pb_{0.10}Te)_{1-x}(Cu_2Te)_x$. a) Temperature-dependent $\kappa_{lat,}$ b) Compared the κ_{lat} of $(Ge_{0.84}Cd_{0.06}Pb_{0.10}Te)_{0.99}(Cu_2Te)_{0.01}$ in this work with other reported GeTe materials. [26,32–34,37,39] c) The calculated κ_{lat} by the Debye–Callaway model. d) Raman spectra of $(Ge_{0.84}Cd_{0.06}Pb_{0.10}Te)_{1-x}(Cu_2Te)_x$. e) Temperature-dependent *ZT* of $(Ge_{0.84}Cd_{0.06}Pb_{0.10}Te)_{1-x}(Cu_2Te)_x$. f) Compared the *ZT* of $(Ge_{0.84}Cd_{0.06}Pb_{0.10}Te)_{0.99}(Cu_2Te)_{0.01}$ in this work with some superior GeTe materials in the 303-653 K range. [26,32,33,37,45,46] g) Room-temperature Vickers microhardness H_v and comparison with literature data. [15,19,47–49] h) compressive tests and comparison with some typical brittle TE materials, [50–55] the inset shows the schematic diagram of the strengthening mechanisms. Photographs of the tested samples i) before and j) after for compressive tests.

To further validate the superior TE and mechanical performance of optimized $(Ge_{0.84}Cd_{0.06}Pb_{0.10}Te)_{1-x}(Cu_2Te)_x$ materials, a 7-pairs of TE modules were assembled, based on $(Ge_{0.84}Cd_{0.06}Pb_{0.10}Te)_{0.99}(Cu_2Te)_{0.01}$ as *p*-type legs and $Yb_{0.3}Co_4Sb_{12}$ (Figure S15) as *n*-type legs, to confirm its mid-temperature TE conversion efficiency. The photo of the module is displayed in the inset of Figure 5b. The output performance test of the module was conducted in a home-built system.[15] The relationship between the output voltage (*U*), output power (*P*), and measured current (*I*) is plotted in Figure 5a. As the ΔT increases, the *U* increases from 0.09 V to 0.92 V, and the *P* also increases. The maximum *P* of 0.4 W (corresponding to power density P_d of 1.47 W cm^{-2}) and a maximum η of ~7.0% are reached at ΔT = 400 K and *I* = 0.87 A (Figure 5b). Moreover, the radiation heat loss during the measurement can lead to an underestimation of η and raise its uncertainty.[59,60] Therefore, power density (P_d) can serve as a reliable parameter to compare the performance of different TE devices, as it is largely independent of radiation heat and heat flux measurements. The P_d obtained in this work surpasses many advanced GeTe-based TE modules,[20,27,61] as well as PbTe-,[62] Cu_2Se-,[63] half-Heusler-,[64] and Skutterudites-based[65] TE modules. It even exceeds 8-pair[61] and 18-pair[20] GeTe/skutterudites TE devices (Figure 5c), and is expected to generate sufficient output power for practical power generation applications. The reduction of the internal resistance R_{in} (Figure

S16) of the TE module and the improvement of the TE performance of *n*-type legs are anticipated to further enhance the η and P_d of the GeTe-based TE module.

On the other hand, the multifunctionality of developing TE materials and the exploration of interdisciplinary fields have always been appealing. In the field of solid-state photonics, lasers are considered the next generation of high-brightness solid-state light sources for optical communication systems. However, the non-radiative recombination generated by high-power laser excitation can produce thermal energy, leading to luminescence failure. In this context, TE materials, driven by their TE conversion, offer a potential solution for harvesting non-radiative energy in high-brightness laser illumination. The enhanced S in this work has strong practical application potential in the nonradiative energy of lasers. A laser power density of ~0.5 W/cm^2 can experimentally generate an output voltage (V), where $V=S\times\Delta T$, of ~0.9 mV (Figure 5d and Figure S17). To optimize energy conversion efficiency, Figure 5e presents a schematic diagram of a modified TE energy harvesting array device. This device utilizes an infrared laser (808 nm) beam with an adjustable power density. Figure 5f displays the transient response curves dependent on the incident power density. Owing to the low thermal conductivity, a large ΔT can be easily established by the photo-TE effect, in conjunction with a large S. As displayed, when the laser power density was increased, the temperature of the illumination spot (temperature on the hot sides) increased, leading to a linear increase in output voltage. When the illumination was terminated, the output voltage returned to its static state. As a result, the TE device displayed a repeatable and stable optical switching behavior, which perfectly aligns with the conditions of laser irradiation (Figure S18).

To explore the scalability of the TE energy harvesting array device and verify its contactless thermosensation function for applications such as smart robotics and augmented reality as human-machine interfaces, we conducted additional tests. When a heat source approaches the center of the TE energy harvesting device, a substantial output voltage can be

rapidly generated (Figure S19), demonstrating its suitability for contactless thermosensation. Furthermore, as shown in Figure 5g, the observed change in output voltage as an object approaches the TE energy harvesting device showcases the device's ability to sense proximity, even when separated from the heat source by several centimeters. Hence, the gradual increase in the response output voltage allows for the detection of the object's proximity to the device. By establishing a specific threshold ($V_{ref\text{-}H}$) as an indicator of thermal sensitivity, following the mechanism of infrared detection, the distance between the TE energy harvesting device and the object serving as the heat source can be determined,[66] thus enabling the contactless thermal sensing function.

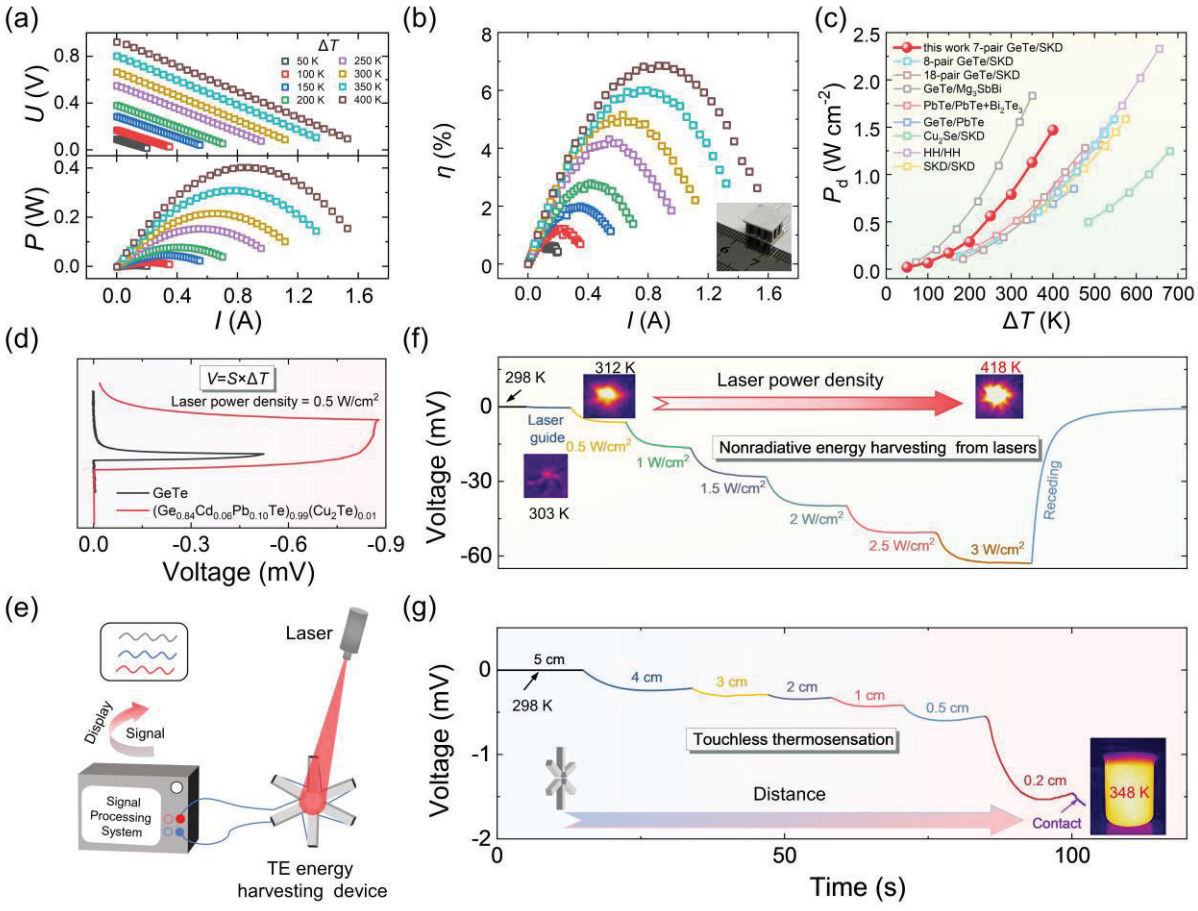

Figure 5 The GeTe-based TE module and TE energy harvesting device. The a) U and P, and b) η of the module as the function of the I at different ΔT. c) Compared the P_d between our TE module and some excellent TE modules,[20,27,61–65,67] where SKD is skutterudites and HH is half-Heusler alloys. d) The photo-

thermoelectric signals of the single-TE energy harvesting module based on the $(Ge_{0.84}Cd_{0.06}Pb_{0.10}Te)_{0.99}(Cu_2Te)_{0.01}$ in this work and the pristine GeTe. e) Schematic diagram of an integrated modular TE energy harvesting device and its sensing signal acquisition circuit. f) The infrared thermal imaging images of infrared radiation correspond to transient photoelectric response curves related to different incident laser power density. g) When the TE energy harvesting device approaches the heat source and records the response voltage change with distance, the inset shows the infrared thermal imaging image of the heat source.

3. Conclusion

In this work, by incorporating Cu_2Te into $Ge_{0.84}Cd_{0.06}Pb_{0.10}Te$, we obtained a competitive ZT of ~2.22 at 803 K and an average ZT_{ave} of ~1.40 in the 303–803 K range in $(Ge_{0.84}Cd_{0.06}Pb_{0.10}Te)_{0.99}(Cu_2Te)_{0.01}$. This is accomplished through a strategy of constructing a coherent nanonetwork across multiple phases, demonstrating applications for TE energy conversion and contactless thermosensation. The Cu_2Te alloying promotes the evolution of defects in the matrix, creating a coherent nanonetwork with multiple nanophases. This coherently improves μ and optimizes n_H to enhance PF, combined with delocalized Cu ions providing a conductive channel for carrier transport. It results in chemical bond softening, effectively blocking phonon transport and significantly enhancing TE performance across the entire temperature range. Moreover, Cu_2Te alloying effectively enhances Vickers microhardness and compressive strength, which is beneficial for the assembly and durability of TE modules. Consequently, a high P_d of ~1.47 W cm^{-2} and a maximum η_{max} of ~7.0% at ΔT = 400 K is attained for the TE module. In particular, the TE energy harvesting array device demonstrates excellent performance in nonradiative energy harvesting of lasers and touchless thermosensation. This study indicates that Cu_2Te alloying effectively optimizes the broad-temperature-range TE performance of GeTe through electron-phonon decoupling, verifying the potential for expanding functions in energy conversion and infrared detection.

Supporting Information

Supporting Information is available from the Wiley Online Library or from the author.

Acknowledgements

We acknowledge the support from the National Key Research and Development Program of China (Grant No. 2018YFA0702100) and the Sichuan University Innovation Research Program of China (Grant No. 2020SCUNL112). Q. S. acknowledges Sichuan Science and Technology Program (Grants No: 2023YFG022, 2023ZYD0064) and Research Funding from West China School/Hospital of Stomatology Sichuan University (Grant No. QDJF2022-2).

Conflict of Interest

The authors declare no conflict of interest.

Data Availability

The data that support the findings of this study are available within the article.

References

[1] L. E. Bell, *Science* **2008**, *321*, 1457.
[2] X.-L. Shi, J. Zou, Z.-G. Chen, *Chem. Rev.* **2020**, *120*, 7399.
[3] G. Tan, L.-D. Zhao, M. G. Kanatzidis, *Chem. Rev.* **2016**, *116*, 12123.
[4] Z. Liu, Y. Wang, T. Yang, Z. Ma, H. Zhang, H. Li, A. Xia, *J. Adv. Ceram.* **2023**, *12*, 539.
[5] J. Zhu, Z. Liu, X. Tong, A. Xia, D. Xu, Y. Lei, J. Yu, D. Tang, X. Ruan, W. Zhao, *ACS Appl. Mater. Interfaces* **2021**, *13*, 23894.
[6] J. Zhu, F. Zhang, X. Tan, R. Li, S. He, R. Ang, *J. Phys.: Condens. Matter* **2023**, *35*, 435503.
[7] Y. Pei, X. Shi, A. LaLonde, H. Wang, L. Chen, G. J. Snyder, *Nature* **2011**, *473*, 66.
[8] X. Zhang, Z. Bu, S. Lin, Z. Chen, W. Li, Y. Pei, *Joule* **2020**, *4*, 986.
[9] M. Hong, M. Li, Y. Wang, X. Shi, Z. Chen, *Adv. Mater.* **2022**, 2208272.
[10] X. Zhang, J. Li, X. Wang, Z. Chen, J. Mao, Y. Chen, Y. Pei, *J. Am. Chem. Soc.* **2018**, *140*, 15883.
[11] J. Li, Z. Chen, X. Zhang, Y. Sun, J. Yang, Y. Pei, *NPG Asia Mater* **2017**, *9*, e353.

[12] J. Li, Z. Chen, X. Zhang, H. Yu, Z. Wu, H. Xie, Y. Chen, Y. Pei, *Adv. Sci.* **2017**, *4*, 1700341.
[13] Z. Bu, W. Li, J. Li, X. Zhang, J. Mao, Y. Chen, Y. Pei, *Mater. Today Phys.* **2019**, *9*, 100096.
[14] S. Duan, W. Xue, H. Yao, X. Wang, C. Wang, S. Li, Z. Zhang, L. Yin, X. Bao, L. Huang, X. Wang, C. Chen, J. Sui, Y. Chen, J. Mao, F. Cao, Y. Wang, Q. Zhang, *Adv. Energy. Mater.* **2022**, *12*, 2103385.
[15] J. Zhu, F. Zhang, Y. Tai, X. Tan, Q. Deng, P. Nan, R. Cheng, C. Xia, Y. Chen, B. Ge, R. Ang, *InfoMat* **2023**, e12514.
[16] Z. Zheng, X. Su, R. Deng, C. Stoumpos, H. Xie, W. Liu, Y. Yan, S. Hao, C. Uher, C. Wolverton, M. G. Kanatzidis, X. Tang, *J. Am. Chem. Soc.* **2018**, *140*, 2673.
[17] M. Hong, W. Lyv, M. Li, S. Xu, Q. Sun, J. Zou, Z.-G. Chen, *Joule* **2020**, *4*, 2030.
[18] L. Wu, X. Li, S. Wang, T. Zhang, J. Yang, W. Zhang, L. Chen, J. Yang, *NPG Asia Mater* **2017**, *9*, e343.
[19] J. Zhu, X. Tan, D. Pan, Y. Luo, R. Li, X. Rao, R. Cheng, C. Xia, Y. Chen, Q. Sun, R. Ang, *Chem. Eng. J.* **2024**, *480*, 148135.
[20] C. Zhang, G. Yan, Y. Wang, X. Wu, L. Hu, F. Liu, W. Ao, O. Cojocaru-Mirédin, M. Wuttig, G. J. Snyder, Y. Yu, *Adv. Energy. Mater.* **2022**, 2203361.
[21] Y. Jiang, J. Dong, H.-L. Zhuang, J. Yu, B. Su, H. Li, J. Pei, F.-H. Sun, M. Zhou, H. Hu, J.-W. Li, Z. Han, B.-P. Zhang, T. Mori, J.-F. Li, *Nat Commun* **2022**, *13*, 6087.
[22] X. Wang, H. Yao, L. Yin, W. Xue, Z. Zhang, S. Duan, L. Chen, C. Chen, J. Sui, X. Liu, Y. Wang, J. Mao, Q. Zhang, X. Lin, *Adv. Energy. Mater.* **2022**, 2201043.
[23] Z. Guo, G. Wu, X. Tan, R. Wang, Z. Zhang, G. Wu, Q. Zhang, J. Wu, G. Liu, J. Jiang, *Adv. Funct. Materials.* **2022**, 2212421.
[24] Y. Qiu, J. Ye, Y. Liu, X. Yang, *RSC Adv.* **2017**, *7*, 22558.
[25] J. Li, F. Mo, L. Guo, J. Huang, Z. Lu, Q. Xu, H. Li, *Sensor. Actua. B: Chem.* **2021**, *328*, 129032.
[26] Q. Zhang, Z. Ti, Y. Zhu, Y. Zhang, Y. Cao, S. Li, M. Wang, D. Li, B. Zou, Y. Hou, P. Wang, G. Tang, *ACS Nano* **2021**, *15*, 19345.
[27] Y. Gelbstein, J. Davidow, S. N. Girard, D. Y. Chung, M. Kanatzidis, *Adv. Energy. Mater.* **2013**, *3*, 815.
[28] Y. Xiao, H. Wu, W. Li, M. Yin, Y. Pei, Y. Zhang, L. Fu, Y. Chen, S. J. Pennycook, L. Huang, J. He, L.-D. Zhao, *J. Am. Chem. Soc.* **2017**, *139*, 18732.
[29] L. You, J. Zhang, S. Pan, Y. Jiang, K. Wang, J. Yang, Y. Pei, Q. Zhu, M. T. Agne, G. J. Snyder, Z. Ren, W. Zhang, J. Luo, *Energy Environ. Sci.* **2019**, *12*, 3089.
[30] C. Zhou, Y. K. Lee, J. Cha, B. Yoo, S.-P. Cho, T. Hyeon, I. Chung, *J. Am. Chem. Soc.* **2018**, *140*, 9282.
[31] J. Li, X. Zhang, X. Wang, Z. Bu, L. Zheng, B. Zhou, F. Xiong, Y. Chen, Y. Pei, *J. Am. Chem. Soc.* **2018**, *140*, 16190.
[32] E. Nshimyimana, S. Hao, X. Su, C. Zhang, W. Liu, Y. Yan, C. Uher, C. Wolverton, M. G. Kanatzidis, X. Tang, *J. Mater. Chem. A* **2020**, *8*, 1193.
[33] L. Xie, Y. Chen, R. Liu, E. Song, T. Xing, T. Deng, Q. Song, J. Liu, R. Zheng, X. Gao, S. Bai, L. Chen, *Nano Energy* **2020**, *68*, 104347.
[34] L. Yin, W. Liu, M. Li, D. Wang, H. Wu, Y. Wang, L. Zhang, X. Shi, Q. Liu, Z. Chen, *Adv Funct Materials* **2023**, *33*, 2301750.
[35] M. Grundmann, *The Physics of Semiconductors: An Introduction Including Nanophysics and Applications*, Springer International Publishing, Cham, **2016**.
[36] C. Zhou, Y. Yu, X. Zhang, Y. Cheng, J. Xu, Y. K. Lee, B. Yoo, O. Cojocaru-Mirédin, G. Liu, S. Cho, M. Wuttig, T. Hyeon, I. Chung, *Adv. Funct. Mater.* **2020**, *30*, 1908405.
[37] M. Hong, Y. Wang, W. Liu, S. Matsumura, H. Wang, J. Zou, Z. Chen, *Adv. Energy Mater.*

2018, *8*, 1801837.
[38] L. You, Y. Liu, X. Li, P. Nan, B. Ge, Y. Jiang, P. Luo, S. Pan, Y. Pei, W. Zhang, G. J. Snyder, J. Yang, J. Zhang, J. Luo, *Energy Environ. Sci.* **2018**, *11*, 1848.
[39] L. Yin, W. Liu, M. Li, Q. Sun, H. Gao, D. Wang, H. Wu, Y. Wang, X. Shi, Q. Liu, Z. Chen, *Adv. Energy Mater.* **2021**, *11*, 2102913.
[40] J. Callaway, H. C. von Baeyer, *Phys. Rev.* **1960**, *120*, 1149.
[41] A. Pawbake, C. Bellin, L. Paulatto, K. Béneut, J. Biscaras, C. Narayana, D. J. Late, A. Shukla, *Phys. Rev. Lett.* **2019**, *122*, 145701.
[42] C. Bellin, A. Pawbake, L. Paulatto, K. Béneut, J. Biscaras, C. Narayana, A. Polian, D. J. Late, A. Shukla, *Phys. Rev. Lett.* **2020**, *125*, 145301.
[43] S. Yang, F. Sui, Y. Liu, R. Qi, X. Feng, S. Dong, P. Yang, F. Yue, *Nanoscale* **2023**, *15*, 13297.
[44] L. Wang, S. Fang, J. Li, L. Hu, F. Liu, W. Xu, T. Mori, C. Zhang, *Cell Rep. Phys. Sci.* **2022**, 101009.
[45] N. Man, J. Cai, Z. Guo, G. Liu, P. Sun, H. Wang, Q. Zhang, X. Tan, Y. Yin, J. Jiang, *ACS Appl. Energy Mater.* **2021**, *4*, 4242.
[46] Y. Jin, D. Ren, Y. Qiu, L. Zhao, *Adv Funct Materials* **2023**, 2304512.
[47] J. Davidow, Y. Gelbstein, *Journal of Elec Materi* **2013**, *42*, 1542.
[48] C. Liu, Z. Zhang, Y. Peng, F. Li, L. Miao, E. Nishibori, R. Chetty, X. Bai, R. Si, J. Gao, X. Wang, Y. Zhu, N. Wang, H. Wei, T. Mori, *Sci. Adv.* **2023**, *9*, eadh0713.
[49] S. Zhi, J. Li, L. Hu, J. Li, N. Li, H. Wu, F. Liu, C. Zhang, W. Ao, H. Xie, X. Zhao, S. J. Pennycook, T. Zhu, *Adv. Sci.* **2021**, *8*, 2100220.
[50] D. Bao, J. Chen, Y. Yu, W. Liu, L. Huang, G. Han, J. Tang, D. Zhou, L. Yang, Z.-G. Chen, *Chem. Eng. J.* **2020**, *388*, 124295.
[51] J. Qiu, Y. Yan, T. Luo, K. Tang, L. Yao, J. Zhang, M. Zhang, X. Su, G. Tan, H. Xie, M. G. Kanatzidis, C. Uher, X. Tang, *Energy Environ. Sci.* **2019**, *12*, 3106.
[52] X. Shi, W. Liu, A. Wu, V. T. Nguyen, H. Gao, Q. Sun, R. Moshwan, J. Zou, Z. Chen, *InfoMat* **2020**, *2*, 1201.
[53] K. Tyagi, B. Gahtori, S. Bathula, M. Jayasimhadri, S. Sharma, N. K. Singh, D. Haranath, A. K. Srivastava, A. Dhar, *Solid. State. Commun.* **2015**, *207*, 21.
[54] L. Zhang, W. Wang, B. Ren, Y. Yan, *Journal of Elec Materi* **2011**, *40*, 1057.
[55] L. Zhang, G. Rogl, A. Grytsiv, S. Puchegger, J. Koppensteiner, F. Spieckermann, H. Kabelka, M. Reinecker, P. Rogl, W. Schranz, M. Zehetbauer, M. A. Carpenter, *Mater Sci Eng B.* **2010**, *170*, 26.
[56] J. Y. He, W. H. Liu, H. Wang, Y. Wu, X. J. Liu, T. G. Nieh, Z. P. Lu, *Acta. Mater.* **2014**, *62*, 105.
[57] Z. Li, S. Ma, S. Zhao, W. Zhang, F. Peng, Q. Li, T. Yang, C.-Y. Wu, D. Wei, Y.-C. Chou, P. K. Liaw, Y. Gao, Z. Wu, *Mater. Today.* **2023**, *63*, 108.
[58] H. Yang, L. Wu, X. Feng, H. Wang, X. Huang, B. Duan, G. Li, P. Zhai, Q. Zhang, *Small* **2024**, 2310692.
[59] G. Bai, Y. Yu, X. Wu, J. Li, Y. Xie, L. Hu, F. Liu, M. Wuttig, O. Cojocaru-Mirédin, C. Zhang, *Adv. Energy. Mater.* **2021**, *11*, 2102012.
[60] S. Roychowdhury, T. Ghosh, R. Arora, M. Samanta, L. Xie, N. K. Singh, A. Soni, J. He, U. V. Waghmare, K. Biswas, *Science* **2021**, *371*, 722.
[61] L. Xie, C. Ming, Q. Song, C. Wang, J. Liao, L. Wang, C. Zhu, F. Xu, Y.-Y. Sun, S. Bai, L. Chen, *Sci. Adv.* **2023**, *9*, eadg7919.
[62] B. Jia, Y. Huang, Y. Wang, Y. Zhou, X. Zhao, S. Ning, X. Xu, P. Lin, Z. Chen, B. Jiang, J. He, *Energy Environ. Sci.* **2022**, *15*, 1920.
[63] P. Qiu, T. Mao, Z. Huang, X. Xia, J. Liao, M. T. Agne, M. Gu, Q. Zhang, D. Ren, S. Bai,

X. Shi, G. J. Snyder, L. Chen, *Joule* **2019**, *3*, 1538.
[64] Y. Xing, R. Liu, J. Liao, Q. Zhang, X. Xia, C. Wang, H. Huang, J. Chu, M. Gu, T. Zhu, C. Zhu, F. Xu, D. Yao, Y. Zeng, S. Bai, C. Uher, L. Chen, *Energy Environ. Sci.* **2019**, *12*, 3390.
[65] J. Chu, J. Huang, R. Liu, J. Liao, X. Xia, Q. Zhang, C. Wang, M. Gu, S. Bai, X. Shi, L. Chen, *Nat Commun* **2020**, *11*, 2723.
[66] X. Guo, X. Lu, P. Jiang, X. Bao, *Adv. Mater.***2024**, 2313911.
[67] Z. Bu, X. Zhang, Y. Hu, Z. Chen, S. Lin, W. Li, Y. Pei, *Energy Environ. Sci.* **2021**, *14*, 6506.